

ON THE ROLE OF AMBIENT REACTIVE PARTICLES IN THE MIXING AND AFTERBURN BEHIND EXPLOSIVE BLAST WAVES

K. Balakrishnan and S. Menon

*School of Aerospace Engineering, Georgia Institute of Technology, Atlanta,
Georgia, USA*

A hybrid two-phase numerical methodology is used to study the propagation of explosive blast waves from spherical charges of TNT and their interaction with an ambient dilute distribution of aluminum particles. The presence of these particles is found to cause perturbations at the contact surface between the inner detonation products and the outer shock-compressed air, which results in Rayleigh-Taylor instabilities at the contact surface. These instabilities grow in time, thereby creating a mixing layer characterized by enhanced mixing between the detonation products and air, resulting in afterburn. The afterburn energy release is observed to affect the pressure decay rate behind the blast wave and the speed and the strength of the secondary shock. The passage of the secondary shock through the mixing layer results in a Richtmyer-Meshkov instability, which is characterized by the creation of vorticity in the mixing layer through baroclinic torque effects. This phenomenon is observed to sustain the mixing process subsequently. The amount of mixing and afterburn are investigated for a range of aluminum particle sizes, mass loading, and initial distribution, and the role played by these particles in the growth of hydrodynamic instabilities is studied. It is shown that for the range of sizes investigated, particle size does not play a significant role in the mixing, but the initial distribution and mass loading do have appreciable impact. Furthermore, the late stages of the afterburn are observed to be self-similar, and independent of the initial triggering of the hydrodynamic instabilities. This study has provided some useful insights on the instabilities induced by ambient reactive particles in detonation flowfields and establishes a simulation capability to study turbulent two-phase processes in an explosive environment.

Keywords: Afterburn; Aluminum; Blast Wave; Explosive; Hydrodynamic Instability; Mixing

INTRODUCTION

Although explosions/detonations have been studied for well over a century, due to the complexities involved, several physical phenomena associated with their behavior still remain to be explored. In particular, the flow-field behind the blast wave is not properly understood due to the experimental inaccessibility of the region in the periphery and interior of the fireball of an explosive event. Furthermore, the short time scales associated with the problem under study makes it impossible for in

Received 8 May 2009; revised 2 September 2009; accepted 16 September 2009.

Address correspondence to S. Menon, School of Aerospace Engineering, Georgia Institute of Technology, Atlanta, GA, 30332-0150. E-mail: suresh.menon@aerospace.gatech.edu

situ experimental analysis. Thus, computational simulations offer a capability to simulate and understand the complex physics involved in the propagation of explosive blast waves and detonations. Two of the earliest investigations of explosions are those of Taylor (1950a) and Sedov (1959), both of which having a notable impact on the science of explosions in the investigations to come in later years. Brode (1959) undertook an investigation of the detonation from a TNT charge and explained the formation of the secondary shock and its subsequent interaction with the contact surface. Although these studies were one-dimensional, they are seminal in the field of explosions, and form the basis of our understanding of blast waves.

When a detonation occurs, the outgoing blast wave will heat and set into motion the ambient field as it propagates through it. Simultaneously, a rarefaction wave propagates inward, forcing an outward acceleration of the detonation product gases. The contact surface between the detonation products and the shock compressed air is swept outward, and is hydrodynamically unstable to perturbations due to the large density gradients across it. Any disturbance in the ambient flow-field or behind the blast wave can be perturbed by these moving shock and expansion waves, causing them to grow further. Shock-shear interactions occur and can result in instabilities that can significantly change the post shock flow-fields. The growth of instabilities in the contact surface of an explosive fireball was first reported by Anisimov and Zeldovich (1977, 1983). The authors identified two limiting cases, i.e., when the length scale of the instability is much less than the distance between the primary and secondary shock, referred to as free Rayleigh-Taylor turbulence, and when the scale of the instability is of the same order. Furthermore, they identified that the position of the secondary shock is critical and decides the spatial scale of the initial Taylor modes, and hence, the rate of mixing and afterburn between the detonation products and the shock-compressed air.

Other past studies, notably by Kuhl (1996), have clearly demonstrated that perturbations can result in hydrodynamic instabilities that are multi-dimensional in nature. These instabilities are primarily Rayleigh-Taylor (Taylor, 1950b) at early times, and are caused by the growth of perturbations at the contact surface. If an explosive charge is “hydrodynamically” smooth, instabilities start to grow from the molecular scales. On the other hand, if the surface of an explosive charge is rough, instabilities start to grow from this characteristic scale. In both scenarios, the instabilities grow with time, and result in a turbulent mixing layer between the detonation products at the core and the shock-compressed air, which are separated by the contact surface. The presence of inert/reactive particles, interior or exterior to the charge, can also result in hydrodynamic instabilities, as we will show in this paper, owing to their interaction with the contact surface. During this interaction, momentum and energy are transferred between the two phases, and therefore, the presence of particles can also cause instabilities/perturbations in explosions.

A short while after the detonation event, the inward moving rarefaction wave over-expands the flow, and this gives rise to a secondary shock (Brode, 1959). This secondary shock is initially weak, and is swept outward by the detonation product gases. During this time, the secondary shock strengthens and subsequently implodes inward. When the secondary shock reflects from the origin, it propagates outward and interacts with the Rayleigh-Taylor structures, giving rise to further growth of these hydrodynamic instabilities, this time in the form of

Richtmyer-Meshkov instabilities (Richtmyer, 1960). This type of instability is characterized by a misalignment of pressure and density gradients, which subsequently results in the creation of vorticity through baroclinic effects—a three-dimensional phenomenon. Thus, the flow-field behind explosive blast waves are characterized by hydrodynamic instabilities that cannot be properly represented by simple one-dimensional models.

The growth of hydrodynamic instabilities has been studied in the past by Kuhl et al. (1996, 1997) by introducing random Gaussian fluctuations to the gas density profile at the outer surface of a high explosive charge. Four distinct phases were identified: blast wave phase, implosion phase, re-shock phase, and asymptotic mixing phase. The authors also showed the growth of vortical structures by the baroclinic mechanism (misaligned pressure and density gradients), and concluded that most of the afterburn occurs in the asymptotic phase. The behavior of an explosive flow-field in a two-phase medium has also been studied. When reactive (or inert) particles are added to explosives, the detonation product gases heat up the metal particles and subsequently ignite them. The burning of these particles releases energy, which enhances the blast effects of explosive charges. Afterburn of gram-range charges of PETN surrounded by flake aluminum has been investigated in closed volumes (calorimeters) by Kuhl et al. (2006). The authors showed that the mean chamber pressure can be enhanced by such charges, where the high explosive is surrounded by reactive aluminum particles. In another experimental study by Zhang et al. (2007), confined explosions of kilo-range TNT charges were investigated with aluminum present either inside the charge or outside as a surrounding shell. The authors showed that the presence of aluminum contained in a shell outside the charge improved the performance during the early afterburning phase, as compared with charges of the high explosive containing aluminum particles inside. They also showed that both charges result in the same quasi-static explosion overpressure after a long duration. Photographic evidence of hydrodynamic instabilities in a multi-phase explosion (i.e., a heterogeneous explosive charge) has been shown by Frost et al. (2005). In another study, Schwer and Kailasanath (2007) studied the propagation of a blast wave from the detonation of a TNT charge into an ambient distribution of water droplets. Although the focus of this study was only on the primary blast wave, the presence of hydrodynamic instabilities was reported. All of these studies have clearly demonstrated that particles/droplets, reactive and non-reactive alike, play a critical role in the afterburn process involved in the detonation of explosives. However, more research is needed to better understand the complex physics involved in the problem.

Aluminum particles, when present along with explosive blasts, pick up heat either from the detonation products or from the shock compressed air, depending on which side of the contact surface they belong. Once these particles reach their ignition temperature, they start to evaporate and subsequently react in the gaseous phase. This reaction of gaseous aluminum can be by two different means (i.e., aerobic or anaerobic; see Kim et al., 2008). Aerobic reaction refers to the reaction of aluminum with the oxygen in the shock compressed air, while anaerobic reaction refers to its reaction with oxidants in the detonation products (viz., CO_2 and H_2O). It is not possible to determine experimentally what proportions of aluminum combustion behind blast waves occurs aerobically or anaerobically, and thus

computational simulations can play a useful role in explaining the aluminum combustion process behind explosive blast waves. To this end, this paper is also aimed at the investigation of the burning aspects of aluminum particles behind the explosive blasts.

The combustion of a droplet/particle in an ambient flow-field can occur in two regimes: diffusive and kinetic. In the diffusive regime, a droplet/particle starts to evaporate after the surface heats up to a certain ignition temperature, following which the gasified fuel diffuses farther away from the surface until it encounters a surrounding oxidizing gas (say, O_2 , H_2O , or CO_2). A diffusion flame is formed far away from the surface of the droplet/particle, and the energy release from the chemical reaction does not directly feed back to heat the droplet/particle further. The chemical kinetic rates are fast, and the oxidizer diffusion rate is the limiting rate—thus the name “diffusive regime.” On the contrary, in the kinetic regime, the oxidizer diffuses to the surface much faster, and thus the rate limiter is the chemical kinetics (essentially, temperature) at the droplet/particle surface, thereby giving rise to the name “kinetic regime”. As the chemical reaction occurs close to the surface, the chemical energy release can feed back to the surface of the droplet/particle. Good theoretical discussions on these regimes can be found elsewhere (Tanguay et al., 2009; Vulis, 1961). One of the major distinct characteristics of the two regimes is that in the diffusive regime, the combustion time scales as d^2 vis-à-vis d for the kinetic regime, where d denotes the droplet/particle diameter.

The diffusive regime has been extensively studied by the research community, with an established correlation provided by Beckstead (2005). In contrast, studies on the kinetic regime are not well established in literature due to the flame being much closer to the surface of the droplet/particle in this regime, thereby rendering inaccessibility to experimental observation. However, some progress has been made very recently. Bazyn et al. (2007) experimentally studied aluminum particle combustion in a shock tube and concluded that particle diameters below $10\text{ }\mu\text{m}$ exhibit transition from the diffusive regime. Furthermore, they also reported the dependence of the aluminum burning time on the oxidizer used, on the percentage of oxidizer in the ambient gas, and the pressure dependence of the burning time. Even experiments conducted by another research group (Shoshin & Dreizin, 2003; Trunov et al., 2005) suggest deviations from the classical diffusive regime for small particle sizes. Recently, Tanguay et al. (2009) undertook an experimental/numerical study of aluminum particle combustion in high-speed detonation products. They extended the conclusion of Bazyn et al. (2007) by emphasizing the role played by convection in the transition of the particle size that demarcates the two regimes. In the present study, the diffusive regime will be used for its simplicity and for being better established. Our primary focus is to elucidate the gas phase flow-field, and thus we believe the choice of the aluminum combustion model will not alter the gas-phase flow physics significantly. This is due to the reaction delay times of aluminum particles used in the current study ($10\text{--}100\text{ }\mu\text{m}$ radius) being on the order of 0.5 msec and above (see Figure 8 of Tanguay et al., 2009), which is much larger than particle-gas interaction time scales ($\sim 0.03\text{ msec}$). In the future, we will be revisiting the kinetic regime for similar problems.

While the role of initial perturbations to the growth of hydrodynamic instabilities behind explosive blasts has been investigated in the aforementioned studies

(Kuhl, 1996; Kuhl et al., 1997), the role of ambient solid particles on the same has not been addressed in the literature. In this paper, we study numerically the detonation of condensed phase explosives with a shell of Al particles outside the charge with a primary focus to investigate the interaction between shock, density interface, particles, and the afterburn process. The impact of these processes on the hydrodynamic instabilities is also addressed. In this study, the amount of aluminum used is very dilute (~ 0.01 – 0.04% initial volume fraction) and serve the purpose of a seed for perturbing the contact surface to trigger the growth of hydrodynamic instabilities. The ignition of aluminum particles is delayed, and many of the particles that ignite quench subsequently as they leave the mixing layer, as we will show later in this study. Thus, the energy involved in the burning of aluminum occurs slowly over a wider time span when compared to the energy release from the afterburning detonation products.

The main objectives of this paper are to characterize the mixing and post-detonation afterburn behavior of explosives due to an ambient distribution of aluminum particles. Emphasis is laid on the elucidation of the conditions under which more mixing and afterburn occur due to the hydrodynamic instabilities triggered by the ambient particles. This paper is organized as follows: in the next section, the governing equations and numerical methodology are presented. Later, the results from the current study are reported and the involved physics elucidated. Finally, the conclusions drawn from this research effort are presented.

GOVERNING EQUATIONS AND NUMERICAL METHOD

Gas Phase

The three-dimensional simulations are conducted using the unsteady, compressible, reacting, multi-species Navier-Stokes equations, and are summarized as follows:

$$\frac{\partial}{\partial t} \begin{bmatrix} \rho \\ \rho u_i \\ \rho E \\ \rho Y_k \end{bmatrix} + \frac{\partial}{\partial x_j} \begin{bmatrix} \rho u_j \\ \rho u_i u_j + p \delta_{ij} - \tau_{ij} \\ (\rho E + p) u_j - u_i \tau_{ji} + q_j \\ \rho Y_k (u_j + V_{j,k}) \end{bmatrix} = \begin{bmatrix} 0 \\ 0 \\ 0 \\ \dot{\omega}_k \end{bmatrix} + \begin{bmatrix} \dot{\rho}_p \\ \dot{\mathbf{F}}_{p,i} \\ \dot{\mathbf{Q}}_p + \dot{\mathbf{W}}_p \\ \dot{\mathbf{S}}_{p,k} \end{bmatrix} \quad (1)$$

where ρ denotes the density, u_i is the i -th component of velocity, E is the specific total energy given by the sum of the internal (e) and the kinetic energy, $e + \frac{1}{2} u_i u_i$, p is the pressure, Y_k is the mass fraction of the k -th species, and the chemical production of the k -th species is represented by $\dot{\omega}_k$. Denoting the total number of chemical species as N_s , the index k in the species equation varies as $k = 1, \dots, N_s$. The stress tensor is denoted by τ_{ij} , j -direction heat flux by q_j , and the j -component diffusion velocity by $V_{j,k}$. The shear stress is obtained as

$$\tau_{ij} = \mu \left(\frac{\partial u_i}{\partial x_j} + \frac{\partial u_j}{\partial x_i} \right) + \delta_{ij} \lambda \frac{\partial u_j}{\partial x_j}, \quad (2)$$

where μ represents the viscosity of the gas phase, obtained from the Sutherland's law, δ_{ij} is the Kronecker delta, and λ denotes the coefficient of bulk viscosity, taken as $-\frac{2}{3}\mu$. The heat flux is obtained as

$$q_j = -\kappa \frac{\partial T}{\partial x_j} + \rho \sum_{k=1}^{N_s} h_k Y_k V_{j,k}, \quad (3)$$

where T denotes the temperature, κ is the thermal conductivity, and h_k is the specific enthalpy for the k -th species. The diffusion velocity is computed from Fick's law—i.e., $V_{j,k} = -D_k/Y_k (\partial Y_k/\partial x_j)$, where D_k denotes the diffusion coefficient of the k -th species, obtained from unity Schmidt number assumption. The last bracket on the right-hand side of Eq. (1) represents the inter-phase coupling terms, to be discussed shortly. Furthermore, the volume occupied by the particles in this study is inconsequential when compared to the gas, and so we assume the entire volume to be exclusively available to the gas (i.e., the gas volume fraction is unity.)

Following recent studies, we use the Noble-Abel equation of state (Johnston, 2005; Kim et al., 2008; Schwer & Kailasanath, 2007), given by

$$p = \frac{\rho RT}{1 - An}, \quad (4)$$

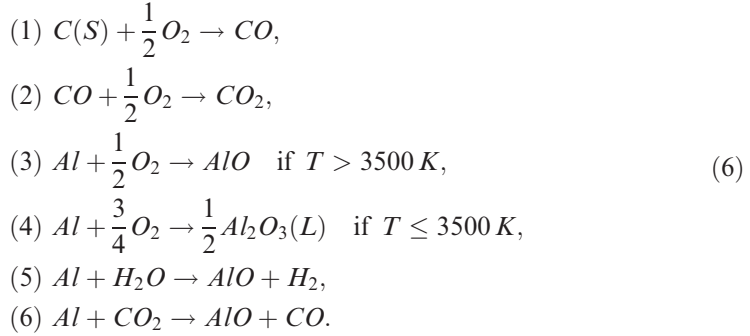
where R denotes the gas constant, n is the number of moles per unit volume, and A is an empirical constant. The speed of sound (a) for a Noble-Abel gas is given by

$$a = \frac{1}{1 - An} \sqrt{\gamma RT}, \quad (5)$$

where γ denotes the ratio of the specific heats. The Noble-Abel equation of state is chosen for the present study mainly because of its simplicity, and for its transition to the ideal gas equation of state for lower densities. The empirical constant, A , is determined from two criteria: ensuring the term $1 - An$ always remains positive; and from a priori knowledge of the blast wave overpressure for a detonation case without particles.

The chemical source term $\dot{\omega}_k$, which arises due to combustion/afterburn, has to be determined. Due to the very high temperatures and pressures involved in the problem under study, the conventional finite-rate Arrhenius kinetics-based reaction rates are not applicable, as these curve fit expressions are based on very different flow conditions (i.e., relatively lower temperatures and pressures). Moreover, due to the very high pressures involved in the problem under study, the reaction rate can also depend on pressure (Kim et al., 2007), which is not well documented. However, the reaction rates for the problem under study are expected to be very fast, and so, in order to simplify the combustion model, the chemical rates are obtained using infinite rate chemistry. This assumption is generally used to model afterburn in explosives (see, for instance, Kim et al.,

2008; Kuhl et al., 1997; and Schwer & Kailasanath, 2007). For the present study, we use a six-step mechanism:



The third and fourth reactions above represent aerobic and the fifth and sixth reactions represent anaerobic reactions of aluminum. Furthermore, we use temperature-dependent curve-fits for the specific heats, $C_p(T)$ for the species (Gordon & McBride, 1994). Note that we have assumed $C(S)$ and $Al_2O_3(L)$ to exist in the condensed phase, and thus use their respective condensed phase $C_p(T)$ curve-fits.

The simulation code is an established DNS/LES solver for combustion flows (Eggenspieler & Menon, 2004; Menon & Patel, 2006). To enable the precise capture of smooth vortical structures, as well as sharp discontinuities (e.g., shocks, contact surface), the current solver combines a central scheme for smooth flow coupled with a shock-capturing scheme based on MUSCL reconstruction using the Harten-Lax-vanLeer (HLL) approximate Riemann solver by means of a hybrid HLLC/HLLE approach. For brevity, this numerical approach is not discussed here, and the interested reader can refer to other research publications that used the same approach (e.g., Balakrishnan et al., 2009; Genin & Menon, in press).

Detonation Initialization

For the initialization of the detonation profiles within the charge, a one-dimensional simulation is carried out employing the Gas-Interpolated-solid Stewart-Prasad-Asay (GISPA) method for the detonation process (Xu et al., 1997). This method permits time-accurate simulation of detonation from the onset of the initial shock through the completion of the detonation of the high explosive. The GISPA algorithm is robust, as emphasized by its ability to capture the reaction zone as well as the Von Neumann spike. The GISPA method is based upon the reactive Euler equations (Xu & Stewart, 1997) and requires appropriate equations of state for both the condensed explosive and the detonation products (Xu et al., 1997). For the condensed explosive, we employ the Hayes equation of state (Hayes, 1976), while for the detonation products, we use the Jones-Wilkins-Lee (JWL) equation of state (Zukas & Walters, 1998). Furthermore, we use Glaister's (1988) version of the Roe scheme along with MUSCL reconstruction for solving the equations to obtain the initial detonation profile. Figure 1 shows the initial profiles used for the present study corresponding to a 11.8 cm dia. TNT charge.

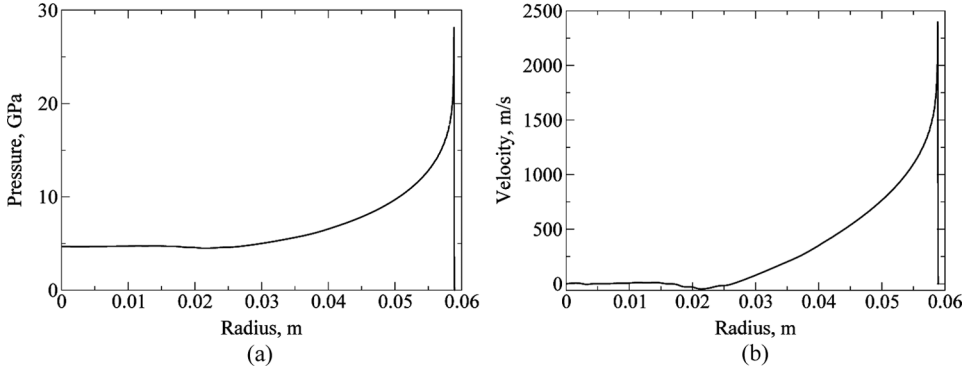


Figure 1 Initial detonation profiles for the TNT charge: (a) pressure, (b) velocity.

Solid Phase

Two-phase flows are generally modeled using a Eulerian approach for both the carrier and dispersed phases, or a Eulerian approach for the carrier and a Lagrangian approach for the dispersed phase; we use the latter in the present study. Newton's law is used to compute the particle kinematics, i.e., the drag force acting on a particle is used to compute the particle velocity vector ($u_{p,i}$). The heat transfer to/from a particle from/to the gas is evaluated assuming convection (Nusselt number) and radiation (Stefan-Boltzman). Under some scenarios, the number of particles to be tracked can be very large, and thus the concept of a parcel is used. Here, a parcel represents a group of particles, each corresponding to the same position, velocity vector, and temperature. Factors like computational cost, available memory, and the desired particle mass loading are used to pre-determine the number of particles per parcel and the total number of parcels required for a simulation. The governing equations for the particle phase are summarized as

$$\frac{dx_{p,i}}{dt} = u_{p,i}, \quad (7)$$

$$\frac{dm_p}{dt} = -\dot{m}_p, \quad (8)$$

$$m_p \frac{du_{p,i}}{dt} = \frac{\pi}{2} r_p^2 C_D \rho_g |u_{g,i} - u_{p,i}| (u_{g,i} - u_{p,i}), \quad (9)$$

$$m_p C_p \frac{dT_p}{dt} = 2\pi r_p \kappa_g Nu (T_g - T_p) - \dot{m}_p L_v + 4\pi r_p^2 \epsilon \sigma (T_g^4 - T_p^4), \quad (10)$$

where m_p is the particle mass, r_p is the particle radius, and ρ_p is the particle material density. Furthermore, C_D represents the drag coefficient and is usually expressed as empirical functions of Reynolds number only for dilute flows (Clift et al., 1978). In the heat transfer equation, C_p denotes the specific heat of the solid particle; κ_g , the thermal conductivity of the gas phase; L_v , the latent heat of vaporization; ϵ , the emissivity, and σ , the Stefan-Boltzman constant. The Nusselt number (Nu) is typically

expressed as empirical functions of Reynolds number and Prandtl number in the literature (Drake, 1961). The system of governing equations for the solid-phase are solved using a fourth-order Runge-Kutta scheme to obtain the solid particle position vector, velocity vector, and temperature. The coupling terms that appear on the right side of the gas phase governing equations (Eq. (1)) are obtained by volume averaging overall the particles/parcels in a finite volume (Vol) and are given by

$$\dot{\rho}_p = \frac{1}{Vol} \sum_1^N n_p \dot{m}_p, \quad (11)$$

$$\dot{F}_{p,i} = \frac{1}{Vol} \sum_1^N n_p \left[\dot{m}_p u_{p,i} + \frac{\pi}{2} r_p^2 C_D \rho_g |u_{p,i} - u_{g,i}| (u_{p,i} - u_{g,i}) \right], \quad (12)$$

$$\dot{Q}_p = \frac{1}{Vol} \sum_1^N n_p \left[\dot{m}_p h_v + 2\pi r_p \kappa_g Nu (T_p - T_g) \right], \quad (13)$$

$$\dot{W}_p = \frac{1}{Vol} \sum_1^N n_p \left[\dot{m}_p u_{p,i} u_{p,i} + \frac{\pi}{2} r_p^2 C_D \rho_g |u_{p,i} - u_{g,i}| (u_{p,i} - u_{g,i}) u_{p,i} \right], \quad (14)$$

$$\dot{S}_{p,k} = \frac{1}{Vol} \sum_1^N n_p \dot{m}_p \text{ (for Al only)}, \quad (15)$$

where N is the total number of parcels in a finite volume cell, n_p is the number of particles per parcel, and h_v denotes the enthalpy change associated with the mass transfer.

When aluminum particles interact with a detonation or blast wave, they can rupture/damage. Some of the discrepancies between computational results and experimental data in literature can be explained by this rupture/damage, as has also been stated by Kim et al. (2007). Particle rupture data are limited and its validity is questionable, prompting us to simplify the problem with the assumption that the aluminum particles remain spherical at all times and that they do not rupture/damage (though we assume the outer aluminum oxide coating ruptures, as is discussed in the next subsection). Furthermore, as mentioned previously, we also assume that the aluminum particle combustion occurs in the diffusive regime; this simplification enables the distinction of evaporation and chemical reaction, both being separable.

Aluminum Evaporation Model

To model aluminum evaporation, an empirical quasi-steady law is used following Kim et al. (2008), Benkiewicz and Hayashi (2006), and Khasainov and Veyssiere (1988):

$$\frac{dr_p}{dt} = -\frac{r_p}{t_b} \left(1 + 0.276\sqrt{Re} \right), \quad (16)$$

where Re denotes the Reynolds number based on the relative velocity between the gas and the particle, and t_b represents a burning time based on the expression $t_b = Kd_p^{o2}$, where d_p^o represents the initial particle diameter, and K , an empirical evaporation constant. In the current study, we choose K as $4 \times 10^6 \text{ sec/m}^2$, following Khasainov and Veyssiere (1988). The mass transfer rate due to evaporation can be obtained as

$$\frac{dm_p}{dt} = -\dot{m}_p = -\frac{d}{dt} \left(\frac{4}{3} \pi \rho_p r_p^3 \right). \quad (17)$$

It is well known that Al particles exist with an oxide coating, which is generally very thin when compared to the particle diameter. This oxide coating plays an important role in the ignition of the aluminum particles. If the coating does not crack open due to physical and/or thermal stresses, the melting point of aluminum oxide ($\sim 2050 \text{ K}$) determines the temperature of ignition. On the other hand, if the oxide coating cracks open, the pure (un-oxidized) aluminum is exposed to the outer gases, and thus the melting point of aluminum ($\sim 950 \text{ K}$) determines the ignition temperature.

Some research studies in the recent past (Gilev & Anisichkin, 2006) have shown that the high gas velocities involved in scenarios similar to the one currently under study result in the aluminum oxide coating to crack open, and thus the melting point of aluminum determines the ignition temperature. Some researchers (e.g., Benkiewicz & Hayashi, 2006) have used 1350 K as the ignition temperature, while others (e.g., Fedorov et al., 2006) have used a value of 900 K . In the present study, we choose 1000 K as the ignition temperature of aluminum. Although this choice is rather ad hoc, we believe that the qualitative conclusions of this study will not depend on the choice of the ignition temperature used. In a numerical study, Benkiewicz and Hayashi (2006) varied the ignition temperature in the range $950\text{--}1500 \text{ K}$ and investigated detonation waves in aluminum-oxygen mixtures. They concluded that although slight quantitative differences exist, the propagation of the detonation wave is not significantly affected. A higher ignition temperature results in a slightly longer time for the particles to start burning. Because the focus of this study is to demonstrate the role played by the ambient particles in the growth of hydrodynamic instabilities, we consider only the said ignition temperature.

RESULTS AND DISCUSSION

The aforementioned hydrodynamic instabilities are critical to the analysis of explosive events such as blast waves and supernovae explosions. All features of interest are related to 3D aspects due to the interaction of perturbations and/or particle motion with the density interface. The density ratio across the contact surface is high ($\sim 500\text{--}1000$) at early times, and is thus very sensitive to the growth of perturbations arising either from imperfections in the explosive grain or from ambient particles. These perturbations grow in time and thus result in a mixing layer between the detonation products and the air, where afterburn occurs. The numerical parameters (viz., simulation domain, grid resolution, etc.) are critical to be able to accurately predict the growth of the hydrodynamic instabilities and the subsequent mixing characteristics; we will now discuss these aspects.

In the current study, we use a spherical sector grid approach for the analysis. Here, we consider only a part of a sphere, i.e., a spherical sector centered about the equator. Very recently, we used this approach to analyze the mixing characteristics involved in the post-detonation afterburn of a TNT charge (Balakrishnan et al., 2009). Others have used this approach to investigate turbulent mixing in spherical implosions (Youngs, 2008). For this sector grid approach, the choice of resolution to be used in the radial (r), azimuthal (θ), and zenith (ϕ) directions is crucial. Our past study (Balakrishnan et al., 2009) shows that a resolution of about 20–25 in the radial direction within the initial charge is required to accurately capture the blast wave and an azimuth/zenith resolution of $\Delta\theta = \Delta\phi = 1^\circ$ to resolve the primary features in the mixing layer. We use 2.4 m long, 45° sector, and a resolution of $1000 \times 45 \times 45$ in r , θ , and ϕ , respectively. We impose free-slip boundary conditions along the sides of the sector and supersonic outflow in the outward plane. The initialization uses the one-dimensional detonation profiles obtained from the GISPA method, as mentioned previously. Because GISPA uses a one-step progress variable approach, the individual species compositions are not obtained; GISPA solves only for the reactants and products as separate entities. The exact detonation product composition (i.e., the individual species; C, CO, H₂O, etc.) composition is still unknown. As a simplification, the products of detonation within the charge and their respective mass fractions are initialized based on the chemical reaction $C_7H_5N_3O_6$ (TNT) $\rightarrow 1.5 N_2 + 2.5 H_2O + 3.5 CO + 3.5 C(S)$.

For all studies, we consider a 11.8 cm dia. spherical TNT charge and use the sector grid. To better understand the role of ambient particles to the mixing characteristics, we also compare the results with those of the same charge without ambient particles to trigger the growth of hydrodynamic instabilities; instead, we add Gaussianly random perturbations to the density (and energy) profiles in the radial region $0.9 r_o \leq r \leq r_o$, where r_o denotes the charge radius, and these serve as the initial seed for the growth of the hydrodynamic instabilities. A similar approach has been used elsewhere (Balakrishnan et al., 2009; Kuhl, 1996; Kuhl et al., 1997). Using this as the baseline case, we compare this to the particle cases to investigate the problem under study. It is emphasized that the GISPA initialization used is more realistic for the problem under study than other means of initialization, such as the constant volume, as the particle interaction with the contact surface occurs immediately outside the initial charge. The gas density in the outer regions of the initial detonation within the charge is about 1800–2200 Kg/m³, different from the constant volume initialization (~ 1630 Kg/m³). Moreover, the initial velocities of the gas in the outer regions of the detonation are about 1800 m/s, compared to rest for the constant volume initialization. Thus, the choice of the initial detonation profile can have a significant role in the early growth of the hydrodynamic structures. However, note that we have used the JWL equation of state for the detonation products in the one-dimensional GISPA detonation simulation, and the Noble-Abel equation of state for the subsequent three-dimensional explosion simulation. In this procedure, the density, pressure, and velocity of the detonation products are conserved during the transition.

In this investigation, focus is laid to explore and understand the following:

1. the role of ambient particles when compared with the particle-free case;
2. the effect of particle size to the mixing characteristics;

3. the effect of initial loading ratio (defined as the ratio of the mass of solid aluminum to the mass of gas in a control volume, denoted η hereafter) to the mixing; and
4. effect of initial radial extent of the particle distribution.

Effect of Initial Perturbations

From past studies, four phases have been identified as critical to the problem: the blast wave phase, implosion phase, re-shock phase, and asymptotic phase (Balakrishnan et al., 2009; Kuhl, 1996; Kuhl et al., 1997). The flow physics in each of these phases will not be elaborated here, and the interested reader is referred to these papers. We consider two sub-cases (viz., low- and high-intensity perturbations added to the initial density (and energy) profiles in the radial region $0.9 r_o \leq r \leq r_o$) and compare the effect of the initial perturbations to the mixing and afterburn characteristics. Specifically, we add Gaussianly generated random perturbations of intensity (max/min) of $\pm 0.1\%$ and $\pm 1\%$, respectively, for the low- and high-intensity perturbation cases to the density in the said radial band of the initial charge. Furthermore, it was confirmed that the mean of the perturbations is almost zero, so that the total mass used to simulate the explosive corresponds to the chosen size. Other means of perturbations can also be used, such as by adding velocity perturbations outside the charge, and we believe the quantitative results will depend on the choice. Because the goal of this investigation is to understand the ensuing mixing process, the sensitivity to the initial choice (density or velocity, etc.) is considered beyond the scope of this paper.

The main distinction between a particle cloud-induced perturbation and that due to Gaussian perturbation is that in the former, the perturbation event occurs continuously (i.e., at multiple time instants). In the latter, the perturbation is introduced at a single time instant, and the hydrodynamic structures are allowed to grow thereafter at an un-forced rate. It does not always mean that a continuously perturbed flow encounters more mixing than an instantaneous perturbation, for if the instantaneous perturbation itself is significantly high enough, it can result in more mixing than a continuously perturbed hydrodynamic growth. In this section, the focus is on mixing and hydrodynamic growth due to initial Gaussian perturbations. Figure 2 shows the mixing layer (isosurface of CO mass fraction) shape at two different times (i.e., Figure 2a and 2b correspond to 0.4 msec; 2c and 2d correspond to 3.5 msec; 2a and 2c correspond to low-intensity initial perturbations; 2b and 2d correspond to high-intensity initial perturbations). During the initial blast wave phase, the structures grow in time, yet preserving their initial perturbation shape (Balakrishnan et al., 2009; Kuhl, 1996). A mixing layer is created where the detonation products and the shocked air mix and burn. During the implosion phase, the secondary shock implodes inward and drags the lower boundary of the mixing layer. The ambient air makes deep incursions into the mixing layer, with afterburn initially occurring only along the edges of these cavities (i.e., where the CO and O₂ mix). More and more air in the inner regions of the mixing layer get consumed, leaving behind pockets of air in the inner regions of the mixing layer that subsequently get consumed by the surrounding C(S)- and CO-rich detonation products.

Subsequently, during the re-shock phase, the secondary shock passes through the mixing layer from the inside and interacts with the density gradients and vortical

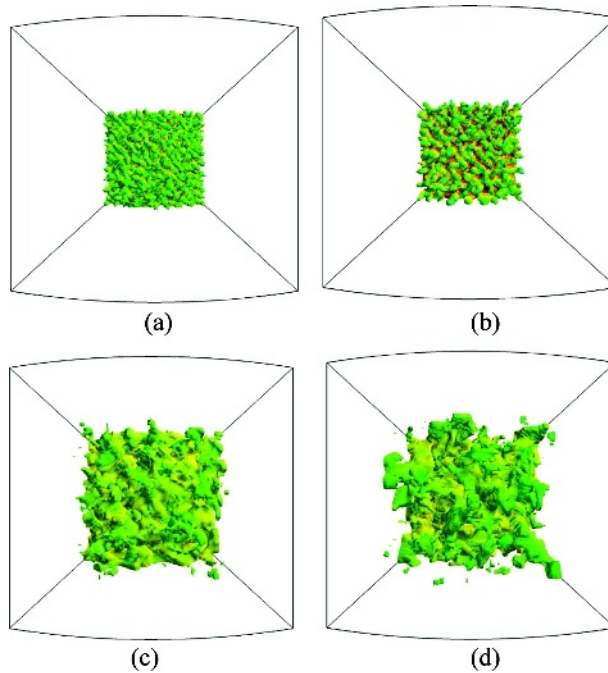


Figure 2 Mixing layer growth at 0.4 msec (a & b) and 3.5 msec (c & d) for the low (a & c) and high (b & d) intensity initial perturbations. Shown here are the CO isosurface contours shaded with the density.

structures in the mixing layer, giving rise to a Richtmyer-Meshkov instability. This is characterized by vorticity creation due to baroclinic effects ($\dot{\omega} = -\nabla(1/\rho) \times \nabla p$), which in turn leads to further mixing enhancement. This baroclinic effect will be revisited and discussed in detail later. Subsequently, in the asymptotic phase, the interaction between contiguous structures and their merging increases, thereby distorting the surface of the mixing layer and giving rise to a wrinkled appearance. During this phase, all the oxygen in the mixing layer has been consumed, and thus the afterburn occurs only near the outer boundary of the mixing layer. Vorticity in the mixing layer causes the merging between contiguous structures, which results in a loss of memory of the initial perturbation shape, as can be observed by comparing Figures 2a and 2c or Figures 2b and 2d, respectively. More detailed discussions on the physics of each of these four phases can be found in the aforementioned references (Balakrishnan et al., 2009; Kuhl, 1996).

Here, we restrict our discussion only to a comparison of the low- and high-intensity initial perturbation cases. From Figures 2a and 2b (i.e., at 0.4 msec time instant), it is observed that the structures are larger but fewer in number for the latter. For the larger initial perturbation intensity, contiguous structures interact and merge earlier; on the other hand, when the initial perturbations are smaller (as the spacing between contiguous structures is greater), they take a longer time to interact and merge. Consequently, the surface area of the structures at 0.4 msec are larger for the case with the larger initial perturbation shape (see Figure 2b), and thus mixing and afterburn are more at 0.4 msec for the larger initial perturbation

case. However, at 3.5 msec, comparing Figures 2c and 2d, the scale and the number of structures are nearly similar for the two cases (i.e., the shape of the structures has attained a self-similarity, independent of the initial perturbation intensity). This time instant corresponds to the asymptotic phase, where the secondary shock has already penetrated through the mixing layer and deposited vorticity through baroclinic effects, which causes the merging and mixing of adjacent structures and results in afterburn. Thus, at late times, the actual scale of the initial perturbations has lost its significance, and fluid mechanic effects like entrainment and vorticity-induced mixing take over. These observations imply that the early-stage mixing and afterburn rates should depend on the scale of the perturbations, with more mixing and afterburn occurring for larger initial perturbations; however, late time mixing and afterburn rates are nearly self-similar and independent of the scale of the initial perturbation size. The only major difference between Figures 2c and 2d are that the latter is slightly more radially “outside” than the former.

To better understand the role of afterburn on the profile of the mixing layer, Figure 3 shows the outer and inner boundaries of the mixing layer, defined here as the radial location where the azimuthally averaged CO mass fraction is $0.1 Y_{\text{CO}}^i$ and $0.9 Y_{\text{CO}}^i$, respectively, where Y_{CO}^i represents the mass fraction of CO at the onset of the completion of detonation within the charge, and is assumed uniform within the charge. Note that this definition is ad hoc and is used only to represent the growth of the mixing layer qualitatively. We normalize the mixing layer boundaries with the initial charge radius, r_o . The observed trend in the mixing layer is discussed elaborately elsewhere (Balakrishnan et al., 2009; Kuhl, 1996); here, we restrict our discussion only to a comparison of the mixing layer profile corresponding to the low- and high-intensity initial perturbations. As observed, the mixing layer is wider for the high-intensity initial perturbation case, as more mixing and afterburn occurs for this case at early times, which expands the gases to a farther radial distance. However, beyond 2 msec, the differences in the mixing layer boundary profiles for the low- and high-intensity perturbations are nearly maintained, emphasizing self-similarity in the late time mixing layer profiles.

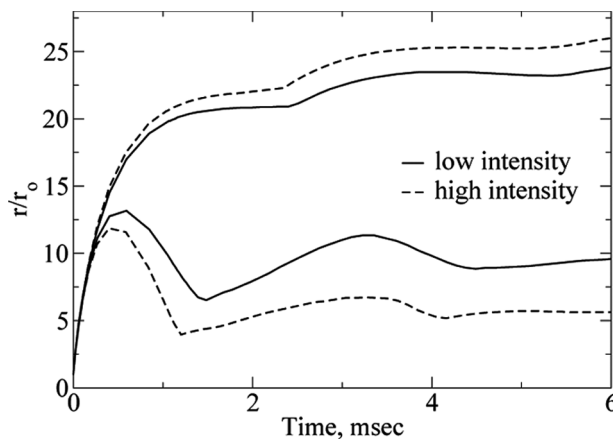


Figure 3 Outer and inner boundaries of the mixing layer with low- and high-intensity initial perturbations.

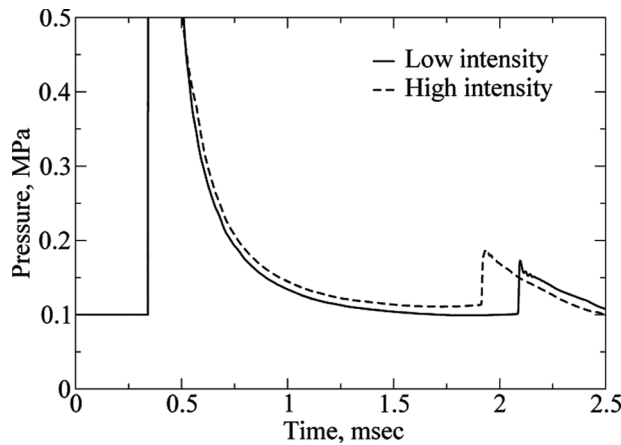


Figure 4 Pressure traces at the 0.9 m radial location for the TNT charge with low- and high-intensity initial perturbations.

The pressure traces at the radial location 0.9 m from the charge center are plotted as a function of time for the two different initial perturbation cases in Figure 4. The time of arrival of the primary shock is identical and independent of the initial perturbations, as the time scale of afterburn energy release is a few orders of magnitude larger than that of the primary blast wave at the 0.9 m location. However, the pressure decay rate behind the primary blast wave is less when the initial perturbation intensity is higher (i.e., around 1.25 msec). Moreover, the time of arrival of the secondary shock is earlier for the high intensity perturbation case, due to the higher afterburn energy release at early times associated with the higher initial perturbation intensity.

Effect of Particle Size

The major difference between mixing induced by the inclusion of random perturbations compared to the mixing induced by ambient particles is that in the former, the contact surface is perturbed instantaneously and the ensuing Rayleigh-Taylor instabilities are allowed to grow without any further triggering mechanism; however, in the latter, the triggering of perturbations/instabilities on the contact surface is undertaken for a finite instant of time, viz., the time period required for the contact surface to overtake the particles. If the particles are sufficiently large, by virtue of their inertia, they are not readily set into motion by the blast wave, thus allowing for the contact surface to overtake them initially. During this instant, inter-phase drag and heat transfer comes into play and creates perturbations on the contact surface that subsequently grow into Rayleigh-Taylor instabilities. The higher the density ratio across the contact surface, the more sensitive it is to the interaction with solid particles. If the particle cloud extends too far radially outward, the outer particles may not have a significant effect on the triggering of perturbations, as the density ratio across the contact surface decreases as it propagates outward. Subsequently, the particles encompassed by the contact surface pick

up momentum from the gas and are set into motion, catching up with the contact surface and interacting with it for a second time. If this second interaction occurs too far radially outward, it may have no significance to the further triggering of perturbations, as the density ratio across the contact surface has decreased considerably.

Specifically, we are interested in particles of radius 10–100 μm in this study. As mentioned previously, the concept of parcel is used, with a certain number of particles assigned to each parcel. Our experience shows that at most 40,000–80,000 parcels are a reasonable choice for acceptable simulation turnaround times and computational memory availability. The number of particles per parcel is chosen based on this requirement and the desired particle mass loading. Stated along these terms, we require 3500, 875, and 56 particles per parcel, respectively, for the 10, 20, and 50 μm particle radius cases (for an initial mass loading ratio, $\eta = 1$, and initial particle distribution extending from outside the charge radius until 25 cm radial distance). For an initial particle distribution extending from outside the charge until 8.68 cm radial distance, the corresponding number of particles per parcel required are 100, 30, and 2, respectively, for the 10, 20, and 50 μm particle radius cases, and $\eta = 1$. Our study shows that the results and the conclusions drawn from the present study are not very sensitive to this choice.

The aforementioned physical phenomena are qualitatively presented in Figure 5, showing the mixing layer and the solid particles at 0.11 and 0.4 msec for the 20 μm particle radius, $\eta = 1$, and an initial particle cloud extending up to 25 cm radial distance. At the earlier time, the particles are seen to interact with the mixing layer, with some particles already being engulfed within the mixing layer; by the later time, the particles have overtaken the mixing layer.

If particles are sufficiently small, by virtue of their lower inertia, a good many of them are set into rapid motion by the blast wave and may not even interact with the contact surface. To study these aspects, we consider a range of particle sizes and investigate their role to the mixing and afterburn process. First, we restrict to a loading ratio, $\eta = 1$, and an initial particle cloud extending from outside the charge radius up to 0.25 m radial distance. Furthermore, we focus only on the mixing and afterburn aspects, and thus do not investigate the dependence of the blast wave

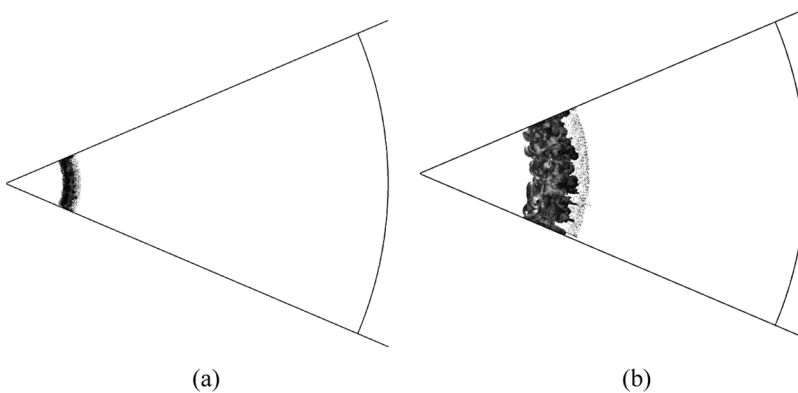


Figure 5 The interaction of solid particles with the mixing layer and their subsequent dispersion at times (a) 0.11 msec, and (b) 0.4 msec.

overpressure on the particle cloud. The interested reader is referred to Schwer and Kailasanath (2007) for a study of the dependence of the blast wave overpressure on ambient water droplets.

We compare the particle-laden cases with the low-intensity Gaussian density perturbations case considered earlier; note that the latter is particle-free and will be the baseline case for the rest of the study. The pressure field behind the blast wave at 0.9 m from the center of the charge is shown in Figure 6 for different particle radii (10–100 μm) along with the baseline case. The pressure decay behind the primary blast wave is less for the cases with particles than the baseline case (see for instance around 1–1.5 msec); furthermore, the secondary shock arrival time is earlier for the particle cases by about 0.25 msec. This is due to the enhanced mixing and afterburn associated with the particle cases in comparison with the baseline case; the additional energy release lowers the pressure decay rates and accelerates the secondary shock. The enhanced mixing for the particle cases is a direct consequence of the longer triggering/stirring of perturbations on the contact surface for the particle cases, with more (longer) triggering made possible with the presence of more particles. Moreover, enhanced mixing directly contributes to enhanced afterburn energy release, thereby resulting in the observed pressure trends and a faster secondary shock.

Another crucial observation from Figure 6 is that the pressure profiles are nearly similar for the different particle sizes considered. Analysis shows that the early Rayleigh-Taylor instabilities caused by the interaction of the contact surface with the particles starts to grow from a scale comparable to the particle size. At later times, the nonlinear growth of the instability loses memory of the initial conditions regardless of the initial particle size, and all cases for different particle sizes, but with the same initial mass loading and initial radial extent of particles give rise to approximately the same pressure field behind the primary blast wave. Thus, although the instabilities may begin from a scale comparable to the particle size, the later time flow physics (entrainment, baroclinic torque, etc.) dictates subsequent mixing and afterburn. These observations are consistently seen in many other simulations (not included here for brevity) and suggest an overall similarity of the flow-field in the

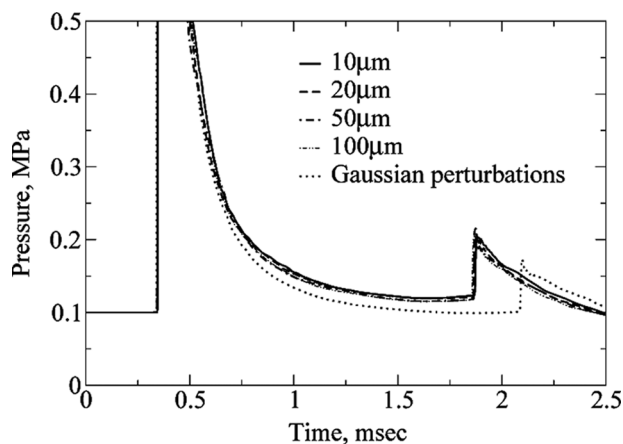


Figure 6 Effect of particle size on the pressure field behind the blast wave.

later stage of the explosion. From a practical point of view, this is an important observation, as it suggests that the late stage observation of the flow-field may not directly correlate to what occurred at the initial stage of explosion in gaseous or particle-laden flow-field. This loss of memory of the Rayleigh-Taylor structures has also been pointed out by Youngs (1984) based on a two-dimensional simulation, albeit in a low-speed, planar, non-reacting, and single-phase flow problem. Very recently, Leinov (2009) undertook an experimental and numerical study of the planar Richtmyer-Meshkov instability and illustrated the significance of the “bubble competition” process. When multi-wavelength hydrodynamic instabilities co-exist on a surface, a bubble competition ensues as contiguous structures start to grow and interact; large bubbles overtake the volume hitherto occupied by the smaller bubbles. Thus, the average wavelength of the hydrodynamic structures increases faster with time, and the width of the multi-wavelength perturbation grows faster vis-à-vis the single-wavelength perturbation.

To quantify the mixing and afterburning rates, Figure 7 shows the mixing layer boundaries and the $C(S)$ mass fraction remaining with time. Here, outer and inner boundaries of the mixing layer are defined as before (radius corresponding to $0.1Y_{CO}^i$ and $0.9Y_{CO}^i$, respectively) and normalized with the initial charge radius, r_o ; mass fractions are defined as the mass of the species remaining normalized by the initial charge mass. As observed in Figure 7a, the mixing layer stretches wider for the particle cases as compared with the baseline particle-free case, due to the longer triggering of the initial perturbations in the former. The outer boundary of the mixing layer is independent of the particle size, although slight differences exist for the inner boundary of the mixing layer. Furthermore, the implosion phase is shorter for the particle cases by about 0.25 msec, as identified by the local minima in the inner boundary of the mixing layer in Figure 7a (1.2 msec for particle cases; 1.45 msec for the baseline case). From Figure 7b, the C consumption rates are faster for the particle cases at early times than the baseline case but are nearly parallel to each other beyond about 1.5 msec, maintaining a constant difference. This indicates that once the mixing and afterburn transform to the outer regions of the mixing layer, they attain a self-similarity and are thenceforth dictated by entrainment which, at late

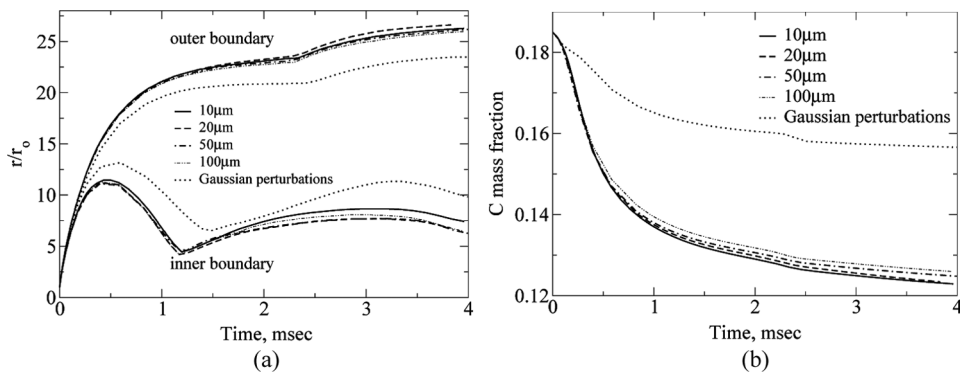


Figure 7 Dependence of mixing and afterburn on particle size: (a) mixing layer boundaries, and (b) C mass fractions remaining.

times, does not depend on the scale at which the very early structures originally grew from (due to memory loss).

Observing the particle evaporation/reaction behavior (not shown here for brevity), it was deduced that large particles ($>50\text{ }\mu\text{m}$ radius) do not ignite due to their large heat transfer time scales. Only intermediate and small particles ignite, and smaller particles subsequently burn longer due to their smaller heat transfer time scales. These conclusions are only valid under the mono-disperse particle size distribution assumption, for in a realistic situation, aluminum particles exist as a distribution of varying sizes. Here, the smaller particles ignite and burn relatively faster, supplying energy to the larger particles and thereby giving rise to the possibility of the ignition of the larger particles. An aluminum particle distribution based on varying particle sizes and their interaction with blast waves will be revisited in the future.

Baroclinic Torque

As mentioned previously, the secondary shock interacts with the structures in the mixing layer during the re-shock phase. This is a Richtmyer-Meshkov instability (Richtmyer, 1960), as the pressure gradients are misaligned with the density gradients, giving rise to the creation of vorticity through the baroclinic mechanism. Here, we demonstrate this physical phenomena and identify its significance to the problem under study. To better understand the creation of vorticity in the mixing layer, we consider the vorticity equation and identify the individual terms that characterize it. The vorticity equation for a compressible flow is summarized as

$$\frac{D\vec{\omega}}{Dt} = (\vec{\omega} \cdot \vec{\nabla}) \vec{V} - \vec{\omega} (\vec{\nabla} \cdot \vec{V}) + \frac{1}{\rho^2} \vec{\nabla} \rho \times \vec{\nabla} p + \vec{\nabla} \times \left(\frac{\vec{\nabla} \cdot \tau}{\rho} \right), \quad (18)$$

where $\vec{\omega}$ is the vorticity vector. The first term on the right side denotes the vortex stretching due to velocity gradients; the second term denotes the vortex stretching due to flow compressibility; and the third term is the baroclinic torque. The last term denotes the diffusion of vorticity due to viscous effects. The baroclinic term is the only source term, and creates vorticity whenever the density and pressure gradients are misaligned, as we will now show with regard to the problem under investigation. The two vortex stretching terms in Eq. (18) contain $\vec{\omega}$, indicating that these terms come into play only if a non-zero vorticity already exists. A vortex subjected to a parallel velocity gradient is bound to stretch, due to which its cross-section decreases; in order to conserve angular momentum, the vorticity magnitude has to increase. This term is critical in the mixing layer behind blast waves, where vortical structures are subjected to large velocity gradients. Furthermore, during the passage of the secondary shock through the mixing layer, the latter is observed to compress, as also reported elsewhere (Balakrishnan et al., 2009; Kuhl, 1996), and thus the vortex stretching due to flow compressibility is also critical in the mixing layer.

To demonstrate the significance of the vortex stretching and the baroclinic terms in the mixing layer during the re-shock phase, Figure 8 shows the three terms: (a) $\ln \left(1 + \left| (\vec{\omega} \cdot \vec{\nabla}) \vec{V} \right| \right)$; (b) $\ln \left(1 + \left| \vec{\omega} (\vec{\nabla} \cdot \vec{V}) \right| \right)$, and (c) $\ln \left(1 + \left| \frac{1}{\rho^2} \vec{\nabla} \rho \times \vec{\nabla} p \right| \right)$ at

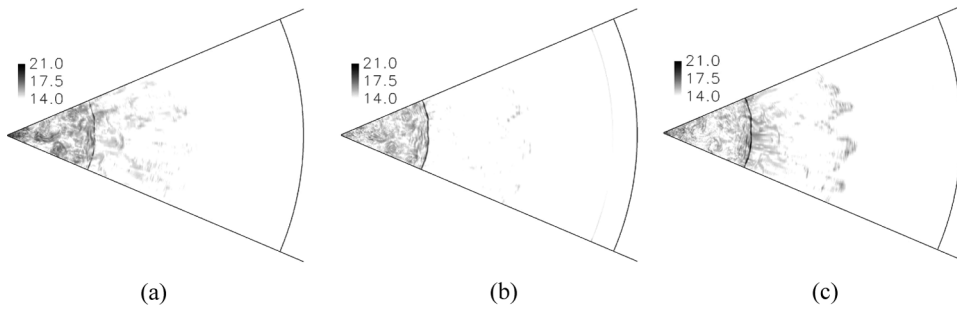


Figure 8 Re-shock phase at 1.6 msec: $\ln(1 + |(\cdot)|)$, where (\cdot) represents (a) vortex stretching due to velocity gradients, (b) vortex stretching due to flow compressibility, and (c) baroclinic term. Units of (\cdot) : sec^{-2} ; see Eq. (18).

1.6 msec for the case corresponding to 50 m particle radius, $\eta = 1$, and an initial particle cloud extending from outside the charge radius up to 25 cm radial distance. From Figure 8c, it is observed that the baroclinic term increases in magnitude as the secondary shock interacts with the structures in the mixing layer, but subsequently decays. This is identified by the thin curved line in the mixing layer in Figure 8c about one-quarter of the radial length of the sector measured from its center. This baroclinic term creates vorticity, which in turn results in vortex stretching as the vortical structures interact with velocity gradients and flow compressibility. Due to this, both the vortex stretching terms sustain even after the passage of the secondary shock, as observed by the “dark regions” behind the secondary shock for both the stretching terms (see Figures 8a and 8b). Furthermore, all of these three terms are of a similar magnitude, thereby indicating that they are all equally important during the re-shock phase. Due to the vorticity creation during the re-shock phase, the secondary shock distorts in shape but re-attains a spherical shape after leaving the mixing layer (not shown here for brevity; see Balakrishnan et al. (2009) for an illustration). The contiguous structures observed to interact in Figure 2 at the later times is a result of this vorticity creation, which further enhances mixing between the inner detonation products and the outer air as the surface area of the structures increase and more air is entrained into the structures.

During the blast wave, implosion, and part of the re-shock phases, afterburn occurs in regions of the mixing layer wherever the pockets/cavities of air interact with the detonation products, and this occurs throughout the width of the mixing layer. Subsequently, all of the oxygen in the mixing layer is consumed, and thus the regions of afterburn are limited to the radially outer regions of the mixing layer due to it being the only region with the availability of oxygen. The flame surface is highly wrinkled, and a similarity exists between the regions of peak CO_2 and temperature, as explained in Balakrishnan et al. (2009). To further sustain burning, the inner detonation products have to mix with the outer air, with the CO_2 formed hitherto being a blanket that separates the two. This later-stage mixing is achieved with the creation of vorticity in the mixing layer by the baroclinic term, and its sustenance thenceforth due to the two vortex stretching terms. It is noteworthy that the first term on the right side of Eq. (18), the vortex stretching due to velocity gradients,

is strictly a three-dimensional term. In two-dimensional flows, the vorticity vector is normal to the plane of the two velocity components, and thus this term vanishes. The vorticity-induced mixing that is critical to sustain afterburn at later times may not be accurately predicted in two-dimensional simulations. Thus, to account for this term, three-dimensional simulations are essential to accurately predict the rate of mixing between the inner detonation products and the outer air.

Mixing Layer/Primary Blast Wave Interaction

Thus far, we have demonstrated the growth of perturbations/instabilities and their subsequent role in the mixing and afterburn process. As these structures propagate radially outward in time, they are decelerated due to spherical spreading. If the deceleration of these structures is less than that of the primary blast wave, it is possible for the structures to catch up with the blast wave, contrary to their behavior as would be predicted by the classical one-dimensional blast wave theory (Sedov, 1959). In particular, if the initial particle distribution causes perturbations sufficiently large, the chances of the ensuing hydrodynamic structures to catch up with the primary blast wave are greater.

To illustrate this phenomenon, we present the density contours at six different instants for the case corresponding to the $10\text{ }\mu\text{m}$ particle radius with $\eta = 1$ and an initial particle distribution extending from outside the charge surface all the way up to 0.25 m in Figure 9, where the figures correspond to early times (i.e., in the range $0.11\text{--}0.58\text{ msec}$). At early times, the hydrodynamic structures lag behind the primary blast wave, as observed in Figure 9a. Subsequently, as observed in Figure 9b, one (or more) of the hydrodynamic structures catches up with the primary blast wave and creates a bump in the latter, more prominently visible in Figure 9c (as indicated by the arrow). During this instant, the pressure behind the blast wave in the vicinity of the penetrating structure is augmented by about 5 bars, as compared with other regions immediately behind the blast wave that are not affected by the hydrodynamic structures. This “bump” or high-pressure spot is created due to the compression of the gas between the outward propagating blast wave and the

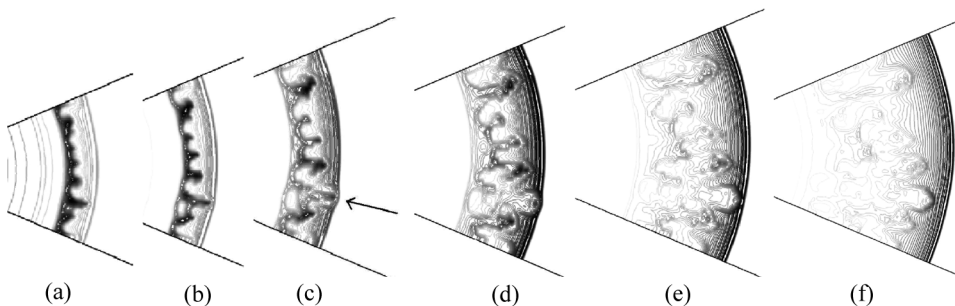


Figure 9 Interaction of the hydrodynamic structures with the primary blast wave: density contours at time instants (a) 0.11 msec, (b) 0.16 msec, (c) 0.22 msec, (d) 0.3 msec, (e) 0.4 msec, and (f) 0.58 msec. Note that the figures are shown in different scale for better clarity.

penetrating structure. Subsequently, the penetrating structure is slowed down more than the blast wave, allowing for the blast wave to re-overtake the structure, as observed in Figure 9e. A distorted blast wave is unstable, and pressure waves propagate in the azimuthal directions from the high-pressure spot, thereby re-sphericalizing the blast wave, as observed in Figure 9f. Our study shows that this early interaction between the hydrodynamic structure and the blast wave does not have any notable long-term impact on the latter. Furthermore, although not verified, we believe that this phenomenon of hydrodynamic structure interaction with the blast wave may not be encountered in planar or cylindrical blast waves, as the decay rate of the blast wave would be lesser as compared with the spherical case considered in this paper.

Effect of Mass Loading

Here, we analyze the effect of the mass loading ratio (η) to the problem under study. The pressure time traces for particles initially extending from outside the charge radius (5.9 cm) up to 8.68 cm radius, for mass loading ratios of $\eta = 0.25$ and 1, are presented in Figure 10. As observed, the pressure decay rate is less, and the secondary shock faster, when the loading ratio is higher, i.e., when more particles are available to perturb the contact surface. The inner and outer boundaries of the mixing layer, as defined before, are shown in Figure 11, with the plain lines corresponding to $\eta = 1$ and the lines with circles corresponding to $\eta = 0.25$ for the case when the initial particle distribution extends from outside the charge radius until 8.68 cm. As observed, the outer boundary of the mixing layer (see Figure 11a) is radially farther by about one charge radius for the $\eta = 1$ case, and is radially farther for both mass loading ratios when compared with the baseline particle-free Gaussian perturbations case. The inner boundary of the mixing layer (see Figure 11b) is radially more “inside” for the particle cases than the baseline case due to more mixing. Furthermore, the inner boundary is more “inside” for the $\eta = 0.25$ case than for $\eta = 1$ at late times, presumably due to more obstruction by the particles for the $\eta = 1$

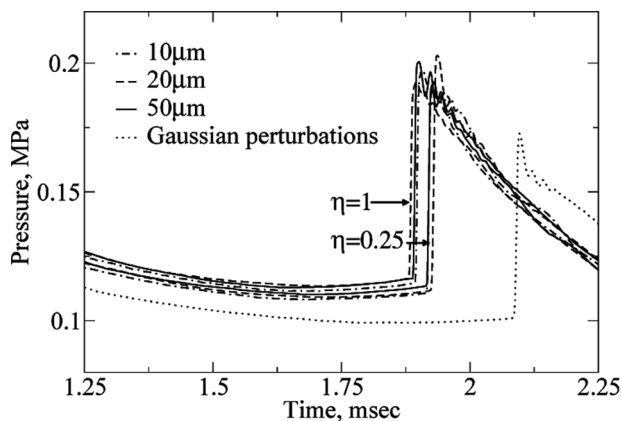


Figure 10 Effect of initial mass loading ratio on the pressure field behind the blast wave.

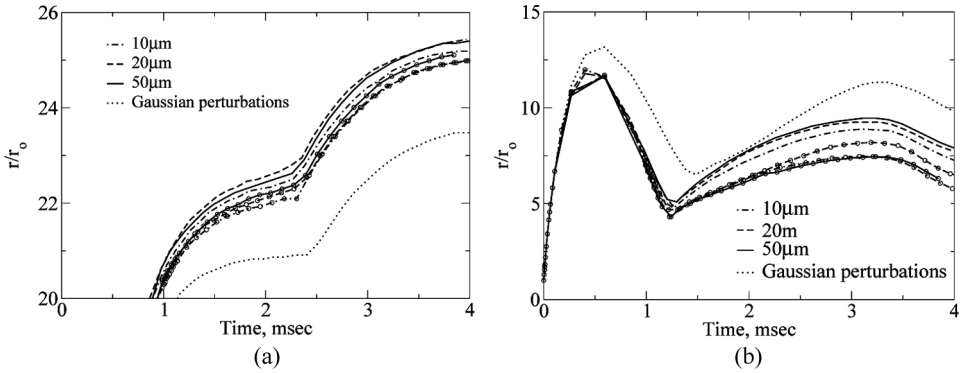


Figure 11 Dependence of mixing layer boundaries on the initial mass loading ratio: (a) outer boundary, (b) inner boundary. The plain lines correspond to $\eta = 1$; the lines with circles correspond to $\eta = 0.25$.

case during the implosion phase (~ 1 msec). However, because the burning transforms to the outer regions of the mixing layer at later times, the inner boundary of the mixing layer loses significance at later times. In summary, this study reveals that the exploding fireball is larger (in terms of outer radius) for the particle cases than the baseline case, indicating that more mixing occurs in the former. Due to this, more afterburn occurs when more ambient particles are available to trigger the early mixing process, as illustrated by the mass fractions of C remaining shown in Figure 12.

Effect of Extent of Particle Distribution

When the initial particle cloud extends radially farther, the contact surface encounters more particles as it propagates outward. Thus, the triggering mechanism for the early Rayleigh-Taylor structures lasts for a longer time duration for a farther

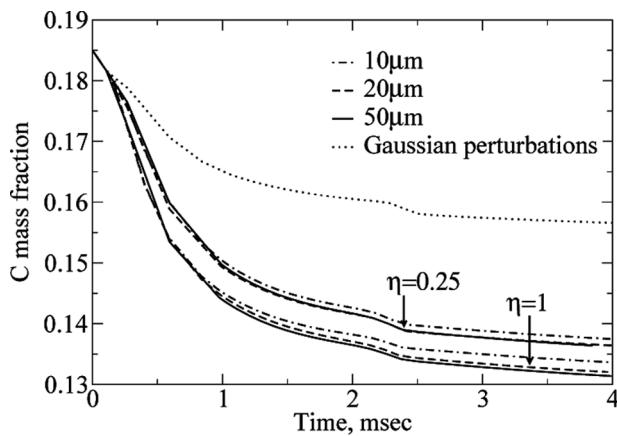


Figure 12 Dependence of afterburn on the initial mass loading ratio: C mass fraction remaining.

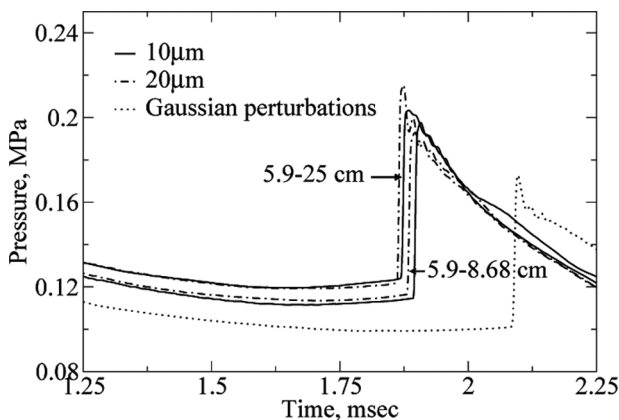


Figure 13 Effect of initial extent of particle distribution on the pressure field behind the blast wave.

initial extent of the particle cloud. To illustrate this fact, Figure 13 shows the pressure-time trace at the 0.9 m radial location for two different initial particle cloud extents, i.e., from outside the charge radius (5.9 cm) up to (i) 8.68 cm and (ii) 25 cm for the same mass loading, $\eta = 1$. We consider different particle radii in the range 10–50 μm and compare the results with the aforementioned particle-free baseline case. As is evident from Figure 13, the pressure decay rates are less when more particles are available to perturb the contact surface (see for instance the time period 1.25–1.5 msec; only 10 and 20 μm size cases are shown here for better clarity). Furthermore, the time of arrival of the secondary shock at this location is earlier by about 0.1 msec for the initial particle extent 5.9–25 cm, in comparison with the 5.9–8.68 cm case, the latter being 0.4 msec earlier than the baseline case with regard to the time of arrival of the secondary shock.

To understand the effect on mixing for a farther extent of the initial particle cloud, Figure 14 shows the outer and inner boundaries of the mixing layer, defined as before. The mixing layer width is clearly wider when more particles are available

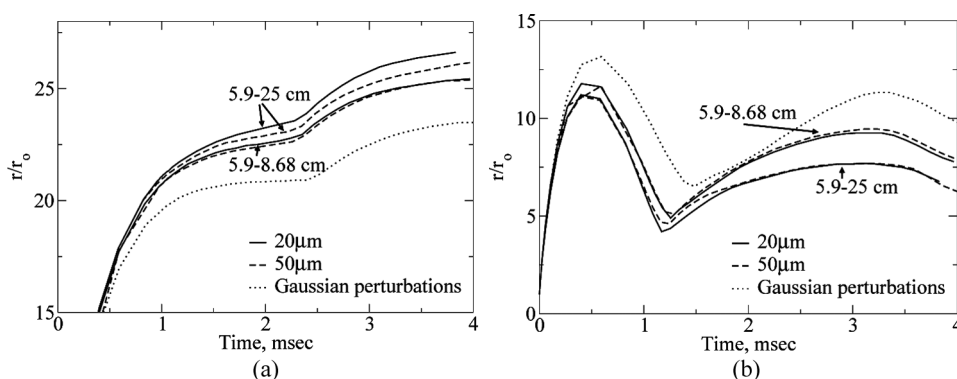


Figure 14 Dependence of mixing layer boundaries on the initial extent of particle distribution: (a) outer boundary, (b) inner boundary.

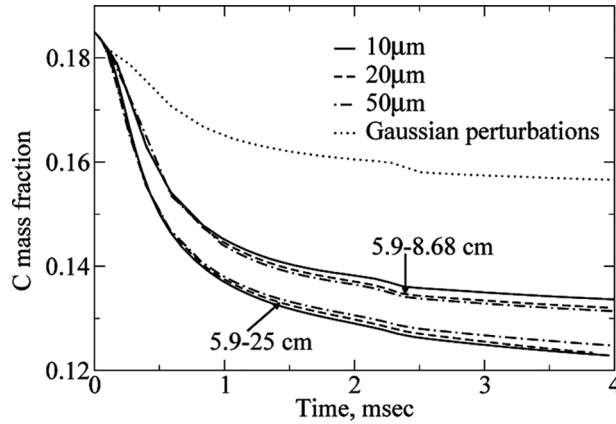


Figure 15 Dependence of afterburn on the initial extent of particle distribution: C mass fraction remaining.

to trigger the early perturbations. Furthermore, the implosion phase is also shorter when more particles are available, as identified by the local minima in the inner boundary of the mixing layer (see time instants 1.2 msec for 5.9–25 cm; 1.4 msec for 5.9–8.68 cm, and 1.5 msec for the baseline case). Thus, more mixing between the inner detonation products and the outer air occurs when more particles are available to perturb the contact surface earlier. This enhanced mixing also relates to enhanced afterburn, as shown by the trends in the C mass fractions remaining in Figure 15. It is interesting to observe, as before, the mass fractions remaining at later times to be nearly parallel for the different cases, thus further emphasizing the self-similarity in the afterburn rates at late times.

Particle Ignition/Quenching

To model the temperature of the aluminum particles, we used the uniform temperature assumption (Eq. (10)), i.e., with the assumption that the conductivity of the particle is infinitely large. With this assumption, the large particles never reach their ignition temperature for the cases considered in this study due to their higher mass. On the other hand, smaller particles readily ignite and burn, anaerobically initially and aerobically later. However, as they subsequently leave the mixing layer, they encounter regions that are relatively cooler and are thus quenched.

To illustrate the evaporation rates of solid aluminum, the time varying solid aluminum mass remaining for the $10\mu\text{m}$ particle radius is shown in Figure 16 normalized with the total initial mass of the aluminum particles. In particular, we focus on the effect of mass loading, η , and the initial width of the particle cloud extending from outside the charge radius (5.9 cm) up to 25 cm and 8.68 cm. As evident from Figure 16, about 60% of solid aluminum remains after being quenched for the shorter initial cloud width, whereas 67% remains with the longer initial cloud. The particles in the outer regions of the longer initial cloud (5.9–25 cm) are set into motion by the leading blast wave and never interact with the afterburning regions

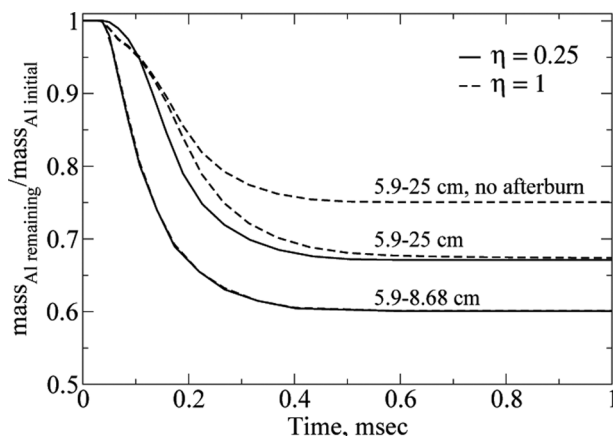


Figure 16 Solid aluminum mass remaining with time.

of the mixing layer, and thus the cloud as a whole evaporates less. On the other hand, shorter initial particle clouds are easily engulfed by the contact surface and thus spend a longer time in the mixing layer, where they can sustain evaporation for a longer time due to availability of heat. Furthermore, it is interesting to note that for the shorter cloud (5.9–8.68 cm), the transient evaporation rates are independent of the mass loading ratio for $\eta = 0.25$ and 1. On the other hand, for the longer cloud (5.9–25 cm), a slightly higher evaporation rate occurs for $\eta = 0.25$ in the time interval 0.12–0.6 msec. This is because the blast wave slows down less for $\eta = 0.25$ as compared with $\eta = 1$, as fewer particles exist in the former, causing higher evaporation rates. However, beyond 0.6 msec, the amount of solid aluminum remaining is identical for both loading ratios ($\sim 67\%$).

To illustrate the significance of the afterburn energy release on the evaporation of aluminum, also shown in Figure 16, is the solid aluminum mass remaining for the $\eta = 1$ case, the initial cloud extending up to 25 cm, but with the afterburn of the detonation products and the gaseous aluminum fictitiously turned off. As observed, about 75% of the solid aluminum remains un-evaporated, implying the dependence of the late-time aluminum evaporation on the afterburn energy release. These findings reveal that ambient solid particles enhance mixing and afterburn of the detonation products, which in turn enhances the evaporation of the particles, i.e., the two phenomena are inter-connected.

We emphasize that these findings conform only to our assumption that aluminum surface reactions are not important, for surface reactions can sustain aluminum particle evaporation even after they leave the mixing layer (see Tanguay et al., 2009, for more discussions on aluminum surface reactions due to its interaction with shock waves). To the best of our knowledge, no experimental data on the amount of aluminum that undergo evaporation/combustion before being quenched exists in the literature with regard to explosive blast waves. The study of aluminum particle combustion as a thermobaric additive to explosives is still in its infancy, and requires more elaborate investigations by the research community to substantiate these observations.

CONCLUSIONS

A robust hybrid numerical methodology is used to study the propagation of explosive blast waves from a spherical TNT charge into reactive aluminum particles in the dilute limit. The presence of these particles is found to cause Rayleigh-Taylor instabilities at the contact surface between the detonation products and the shock-compressed air, which results in enhanced mixing and afterburn. The problem under study is characterized by four distinctive phases, consistent with earlier particle-free studies in which the instabilities were triggered by other means. During the outward passage of the secondary shock through the mixing layer, Richtmyer-Meshkov instabilities are observed, and vorticity is significantly enhanced by the baroclinic torque effect. This creation of vorticity is found to be responsible for contiguous structures to interact, thereby resulting in a loss of memory of the initial shape of the instabilities.

The amount of mixing and afterburn in the mixing layer behind the blast wave is found to be nearly independent of the particle size, but dependent on the initial particle distribution and mass loading. Furthermore, the afterburn energy release is observed to significantly affect the flow-field behind the blast wave. The pressure decay rate behind the primary blast wave is lowered, and the secondary shock is observed to be faster and stronger due to the presence of hydrodynamic instabilities. At late times, the afterburn energy release occurs at the outer regions of the mixing layer, and is observed to be nearly self-similar and independent of the early phase triggering of the hydrodynamic instabilities due to a loss of memory.

The motion, heating, and burning characteristics of the aluminum particles are also investigated and explained. While large particle did not ignite, small particles ignite and subsequently quench. At late times, the evaporation rates are dependent on the afterburn energy release, and on the initial distribution of the aluminum particles. Overall, this study has provided some useful insights on the flow-fields behind explosive blast waves and the hydrodynamic instabilities induced by ambient reactive particles.

ACKNOWLEDGMENTS

This research is supported by the Office of Naval Research (Dr. Cliff Bedford, Program Manager) and the Air Force Research Laboratory (Dr. Douglas Nance, Program Manager). Simulations were carried out at the DoD HPC Centers at the U.S. Army Research Laboratory Major Shared Resource Center and the Maui High Performance Computing Center. Dr Douglas Nance supplied the TNT detonation profiles.

REFERENCES

- Anisimov, S.I., and Zeldovich, Ya.B. 1977. Rayleigh-Taylor instability of boundary between detonation products and gas in spherical explosion. *Pis'ma Zh. Eksp. Teor. Fiz.*, **3**, 1081.
- Anisimov, S.I., Zeldovich, Ya.B., Inogamov, M.A., and Ivanov, M.F. 1983. The Taylor instability of contact boundary between expanding detonation products and a surrounding gas. *Prog. Astro. Aero.*, **87**, 218.

- Balakrishnan, K., Genin, F., Nance, D.V., and Menon, S. 2009. Numerical study of blast characteristics from detonation of homogeneous explosives. *Shock Waves*, DOI: 10.1007/s00193-009-0236-4.
- Bazyn, T., Krier, H., and Glumac, N. 2007. Evidence of the transition from the diffusion-limit in aluminum particle combustion. *Proc. Combust. Instit.*, **31**, 2021.
- Beckstead, M.W. 2005. Correlating aluminum burning times. *Combust. Expl. Shock Waves*, **41**, 533.
- Benkiewicz, K., and Hayashi, A.K. 2006. Parametric studies of aluminum combustion model for simulations of detonation waves. *AIAA J.*, **44**(3), 608.
- Brode, H.L. 1959. Blast wave from a spherical charge. *Phys. Fluids*, **2**, 217.
- Clift, R., Grace, J.R., and Weber, M.E. 1978. *Bubbles, drops and particles*. Academic Press, New York.
- Drake, R.M. 1961. Discussion on the paper entitled "Forced convection heat transfer from an isothermal sphere to water" by G. C. Violet and G. Leppert. *ASME J. Heat Transfer*, **83**, 170.
- Eggenspieler, G., and Menon, S. 2004. Large-eddy simulation of pollutant emission in a DOE-HAT combustor. *J. Propulsion Power*, **20**(6), 1076.
- Fedorov, A.V., Fomin, V.M., and Khmel, T.A. 2006. Theoretical and numerical study of detonation processes in gas suspensions with aluminum particles. *Combust. Expl. Shock Waves*, **42**(6), 735.
- Frost, D.L., Zarei, Z., and Zhang, Z. 2005. Instability of combustion products interface from detonation of heterogeneous explosives. *International Colloquium on the Dynamics of Explosions and Reactive Systems*, July 31–August 5, Montreal, Canada.
- Genin, F., and Menon, S. Dynamics of sonic jet injection into supersonic crossflow. *J. Turbulence*, in press.
- Gilev, S.D., and Anisichkin, V.F. 2006. Interaction of aluminum with detonation products. *Combust. Expl. Shock Waves*, **42**, 107.
- Glaister, P. 1988. An approximate linearized Riemann solver for the Euler equations for real gases. *J. Comput. Phys.*, **74**, 382.
- Gordon, S., and McBride, B.J. 1994. Computer program for calculation of complex chemical equilibrium compositions and applications, I: Analysis. NASA Reference Publication 1311.
- Hayes, D.B. 1976. A $P^n t$ detonation criterion from thermal explosion theory. *Sixth International Symposium on Detonation*, August 24–27, Pasadena, Calif.
- Johnston, I.A. 2005. The Noble-Abel equation of state: Thermodynamic derivations for ballistics modeling. *Defence Sci. Tech. Org.*, DSTO-TN-0670.
- Khasainov, A., and Veyssiere, B. 1988. Steady, plane, double-front detonations in gaseous detonable mixtures containing a suspension of aluminum particles. *Dyn. Expl.: Prog. Astro. Aero.*, **114**, 284.
- Kim, K., Wilson, W., Peiris, S., Needham, C., Watry, C., Ortle, D.J., and Zhang, F. 2007. Effects of particle damage during detonation of thermobarics on subsequent reactions. *International Colloquium on the Dynamics of Explosions and Reactive Systems*, July 23–27, Poitiers, France.
- Kim, C.K., Moon, J.G., Hwang, J.S., Lai, M.C., and Im, K.S. 2008. Afterburning of TNT explosive products in air with aluminum particles. AIAA Paper 2008-1029.
- Kuhl, A.L. 1996. *Spherical mixing layers in explosions: Dynamics of exothermicity*, Gordon and Breach Publishers, Newark, NJ, p. 291.
- Kuhl, A.L., Ferguson, R.E., and Oppenheim, A.K. 1997. Gas dynamic model of turbulent exothermic fields in explosions. *Prog. Astro. Aero.*, **173**, 251.

- Kuhl, A.L., Neuwald, P., and Reichenbach, H. 2006. Effectiveness of combustion of shock-dispersed fuels in calorimeters of various volumes. *Combust., Expl., Shock Waves*, **42**(6), 731.
- Leinov, E., Malamud, G., Elbaz, Y., Levin, L. A., Ben-Dor, G., Shvarts, D., and Sadot, O. 2009. Experimental and numerical investigation of the Richtmyer-Meshkov instability under re-shock conditions. *J. Fluid Mech.*, **626**, 449.
- Menon, S., and Patel, N. 2006. Subgrid modeling for simulation of spray combustion in large-scale combustors. *AIAA J.*, **44**(4), 709.
- Richtmyer, R.D. 1960. Taylor instability in a shock acceleration of compressible fluids. *Comm. Pure Appl. Math.*, **13**, 297.
- Schwer, D.A., and Kailasanath, K. 2007. Numerical simulation of the mitigation of unconfined explosions using water-mist. *Proc. Combust. Instit.*, **31**, 2361.
- Sedov, L.I. 1959. *Similarity and dimensional methods in mechanics*, Academic Press, New York.
- Shoshin, Y., and Dreizin, E. 2003. Particle combustion rates in premixed flames of polydisperse metal-air aerosols. *Combust. Flame*, **133**, 275.
- Tanguay, V., Goroshin, S., Higgins, A.J., and Zhang, F. 2009. Aluminum particle combustion in high-speed detonation products. *Combust. Sci. Tech.*, **181**, 670.
- Taylor, G.I. 1950a. The formation of a blast wave by a very intense explosion. *Proc. Royal Soc. London*, **201**(1), 175.
- Taylor, G.I. 1950b. The instability of liquid surfaces when accelerated in a direction perpendicular to their planes. *Proc. Royal Soc. London. Series A, Math. and Phys. Sci.*, **201**, 192.
- Trunov, M.A., Schoenitz, M., and Dreizin, E.L. 2005. Ignition of aluminum powders under different experimental conditions. *Propellants, Explosives, and Pyrotechnics*, **30**(1), 36.
- Vulis, L.A. 1961. *Thermal regimes of combustion*, McGraw Hill Book Company, New York.
- Xu, S., Aslam, T., and Stewart, D.S. 1997. High resolution numerical simulation of ideal and non-ideal compressible reacting flows with embedded internal boundaries. *Combust. Theor. Model.*, **1**, 113.
- Xu, S., and Stewart, D.S. 1997. Deflagration-to-detonation transition in porous energetic materials: A comparative model study. *J. Eng. Math.*, **31**, 143.
- Youngs, D.L. 1984. Numerical simulation of turbulent mixing by Rayleigh-Taylor instability. *Physica D*, **12**, 32.
- Youngs, D.L., and Williams, R. 2008. Turbulent mixing in spherical implosions. *Int. J. Num. Meth. Fluids*, **56**, 1597.
- Zhang, F., Anderson, J., and Yoshinaka, A. 2007. Post-detonation energy release from TNT-aluminum explosives. *AIP Shock Compr. Cond. Matter*, Waikoloa, Hawaii.
- Zukas, J.A., and Walters, W.P. 1998. *Explosive effects and applications*, Springer, New York.